Electronic Supplementary Information (ESI)

Ultra-efficient energy transfer and near-infrared luminescence in hexagonal aluminate phosphors enabled by heterogeneous ion pairs co-doping

Xiaoyi Liu[1], Zhaojiang Liu[2], Yujuan Dong[2], Chuang Wang[*2], Yichao Wang[*3], Ge Zhu[*4], Shuangyu Xin[4]

[1]*College of Chemistry, Bohai University, Jinzhou, 121000, P. R. China.*

[2]*College of Materials and Environmental Engineering, Bohai University, Jinzhou, 121000, P. R. China.*

[3]*College of Science, Dalian Maritime University, Dalian, 116026, P. R. China.*

[4]*Key Laboratory of New Energy and Rare Earth Resource Utilization of State Ethnic Affairs Commission, College of Physics and Materials Engineering, Dalian Minzu University, 18 Liaohe West Road, Dalian, 116600, P. R. China.*

**Corresponding Author.*

E-mail address: wangchuangbhu@163.com, wangyc2020@dlmu.edu.cn, zhuge06@126.com

Experimental section

Materials and Synthesis of green phosphors

A series of $LaMgAl_{11}O_{19}:xCr^{3+}$ (x = 0%, 0.05%, 0.1%, 0.3%, 0.5%, 0.7% and 0.9%), $LaMgAl_{11}O_{19}:yMn^{2+}$ (y = 0%, 5%, 10%, 15%, 20%, 25%, 30%, 35% and 40%) and $LaMgAl_{11}O_{19}$:20%Mn^{2+}, xCr^{3+} (x = 0%, 0.05%, 0.1%, 0.3%, 0.5%, 0.7% and 0.9%) phosphors were prepared via High temperature solid phase method. In a typical synthesis process of $LaMgAl_{11}O_{19}$:20%Mn^{2+}, 0.5%Cr^{3+}, the raw materials La_2O_3 (99.9%, Macklin), MgO (98.0%, Macklin), Al_2O_3 (99.0% Macklin), $MnCO_3$ (99.95%, Macklin) and Cr_2O_3 (99.9%, Macklin) were weighed stoically and then ground and mixed in an agate mortar. Then mixture was then put into a crucible and sintered in a reducing atmosphere (H_2) at 1600 ℃ for 4 h. Finally, target product was collected after cooling to room temperature. Similarly, all other samples were obtained by the same synthesis method except for stoichiometric ratios.

Characterizations

The phase purity of the as-synthesized samples was performed on a DX-2700BHX X-ray diffractometer (XRD) with Cu Kα radiation (λ = 0.15406 nm). Rietveld refinement of XRD data was carried out on the General Structure Analysis System (GSAS) program. The morphology and composition of the samples were observed via transmission electron microscope (TEM, JEM-F200). The samples were studied by spherical distortion corrected high-angle annular dark-field scanning transmission electron microscope (HAADF-STEM). Element compositions and chemical valence state of the phosphors were detected via X-ray photoelectron spectroscopy (XPS, Axis

Supra+). Excitation spectra, emission spectra and fluorescence decay curves were collected by FLS-1000 fluorescence spectrophotometer equipped with the 150 W xenon lamp as light source. The electron spin resonance (EPR) test was conducted using the Bruker ESR5000 type electron paramagnetic resonance spectrometer (Germany). Take 25 mg of the dried sample and place it in a quartz EPR sample tube (5 mm in diameter). Insert the tube into the center of the resonant cavity, connect it to the low-temperature control system, gradually cool it to 100 K and maintain a stable temperature. Start the scan and record the EPR spectrum. The power is 5.0 mW, attenuation is 13.0 dB, microwave frequency is approximately 9.451389 GHz (X-band). Scanning parameters: sweep time is 30 s, modulation amplitude is 0.20000 mT, modulation frequency is 100 kHz. Photoluminescence quantum yield (PLQY) was collected via the fluorescence spectrophotometer (FLS-1000, Edinburgh Instruments Ltd., UK), in which the $BaSO_4$ powder was used as a reference to determine the absorption. The temperature dependence photoluminescence spectra properties of the as-prepared samples at different temperatures ranging from 25 ℃ to 250 ℃ were estimated by FLS-1000.

Density Functional Theory (DFT) Calculation

The calculation of DFT is carried out in the PBE scheme by the Vienna ab initio simulation package (VASP) software package. The 2×2×2 supercells were established for the following calculations. The projector augment wave (PAW) pseudopotentials are chosen to describe the interactions function of elements. According to the convergence test calculations of host, all the calculation process took a k-point grids of 8×8×2. In addition, the positions of all ions were considered as relaxation when the

residual force was less than 0.01 eV/Å.

Fabrication of LED devices

The as-prepared near-infrared phosphors ($LaMgAl_{11}O_{19}$:0.5%Cr^{3+} or $LaMgAl_{11}O_{19}$:20%Mn^{2+}, 0.5%Cr^{3+}) were first mixed with type A organic resin and type B curing agent, and coated on a 460 nm (1W) blue chips. then the mixtures were cured at 150 ℃ for 2 h to form the final near-infrared pc-LED devices. Full spectrum WLED device was encapsulated by mixing as-synthesized $LaMgAl_{11}O_{19}$:20%Mn^{2+}, 0.5%Cr^{3+} phosphor, commercial $(Ba, Sr)_2SiO_4:Eu^{2+}$ green phosphor, $CaAlSiN_3:Eu^{2+}$ red phosphor, type A organic resin and type B curing agent with 460 nm blue chip (1 W). Electroluminescence performances were measured at 15 V voltage and 50 ~ 350 mA current on the SSP6612 photoelectric measurement system.

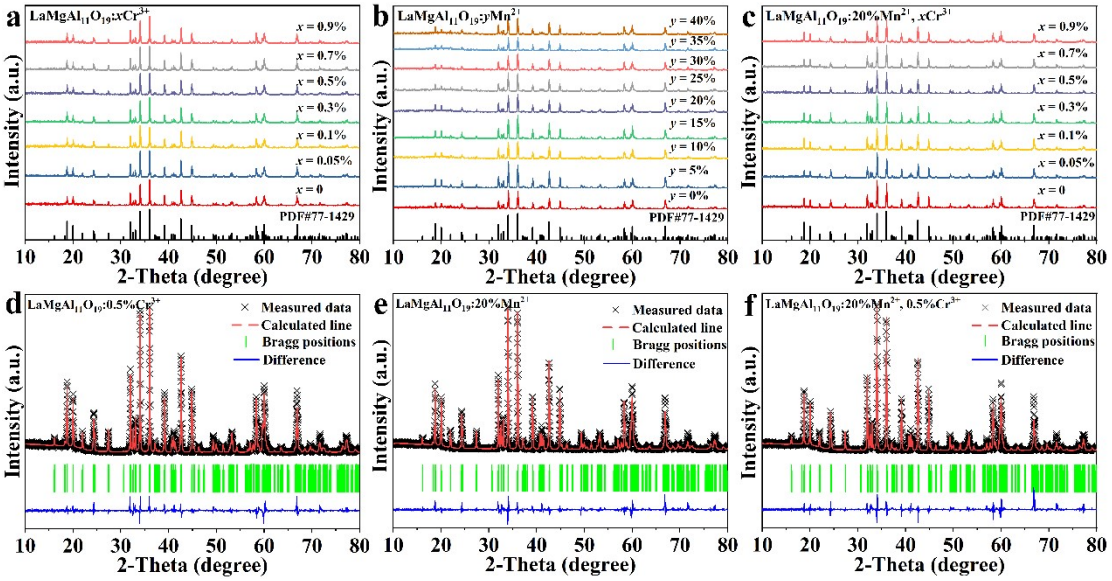

Fig. S1 XRD patterns of $LaMgAl_{11}O_{19}$:$x$$Cr^{3+}$($x$ = 0, 0.05%, 0.1%, 0.3%, 0.5%, 0.7% and 0.9%) (a), $LaMgAl_{11}O_{19}$:$y$$Mn^{2+}$ (y = 0%, 5%, 10%, 15%, 20%, 25%, 30%, 35% and 40%) (b)and $LaMgAl_{11}O_{19}$:20%Mn^{2+}, $x$$Cr^{3+}$ (x = 0, 0.05%, 0.1%, 0.3%, 0.5%, 0.7% and 0.9%) and Rietveld refinement for the typical XRD patterns of $LaMgAl_{11}O_{19}$:0.5%Cr^{3+} (d), $LaMgAl_{11}O_{19}$:20%Mn^{2+} (e)and $LaMgAl_{11}O_{19}$:20%Mn^{2+}, 0.5%Cr^{3+}(f)

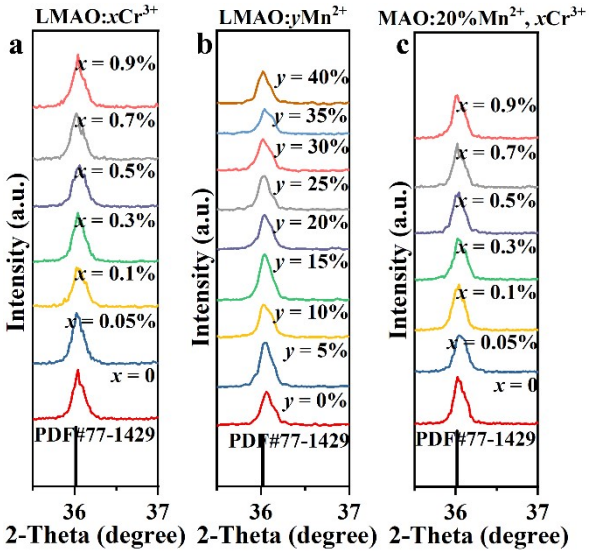

Fig. S2 The magnified XRD curves in the 2θ range of 35.5°-37° of LMAO:xCr^{3+} (x = 0, 0.05%, 0.1%, 0.3%, 0.5%, 0.7% and 0.9%) (a), LMAO:yMn^{2+} (y = 0%, 5%, 10%, 15%, 20%, 25%, 30%, 35% and 40%) (b) and LMAO:20%Mn^{2+}, xCr^{3+} (x = 0, 0.05%, 0.1%, 0.3%, 0.5%, 0.7% and 0.9%) (c)

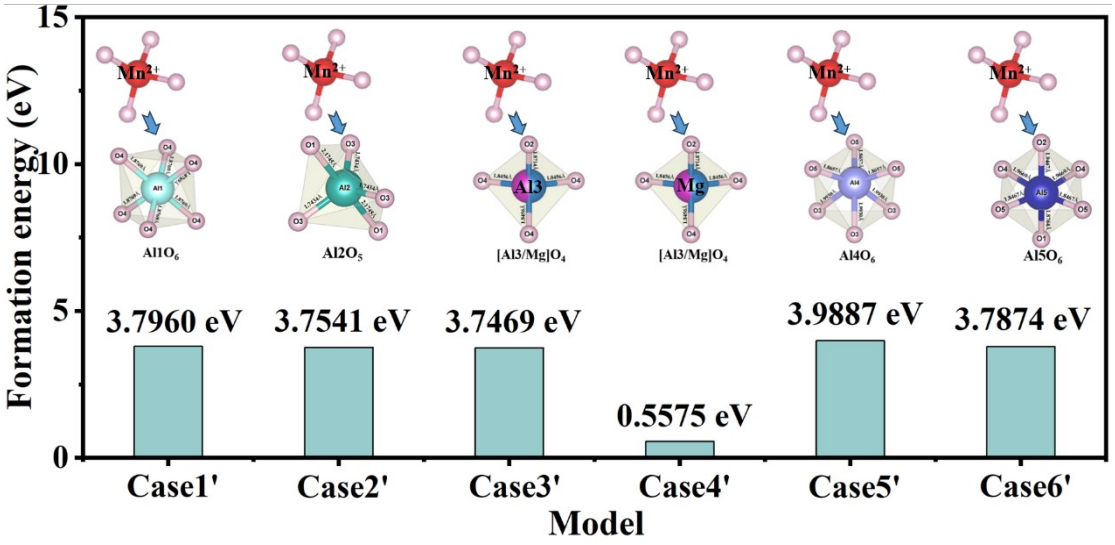

Fig. S3 Formation energy diagram comparing each available doping model in LMAO:Mn^{2+}

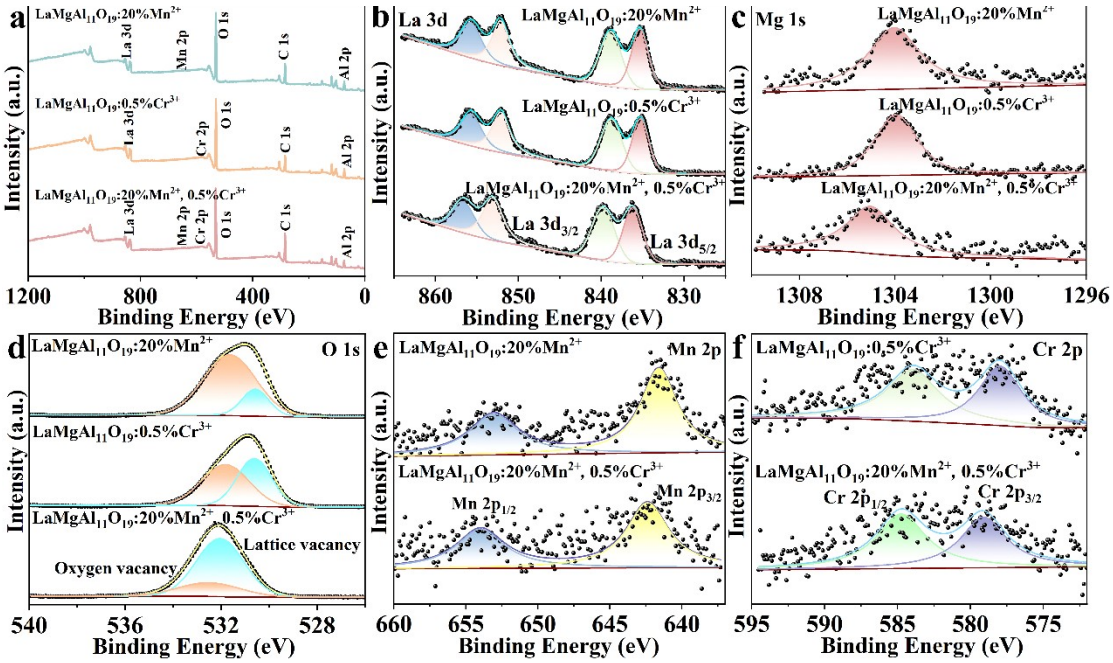

Fig. S4 XPS spectra (a), high resolution XPS spectra of La 3d (b), Mg 1s (c), O 1s (d), Mn 2p (e) and Cr 2p (f) for $LaMgAl_{11}O_{19}$:20%Mn^{2+}, $LaMgAl_{11}O_{19}$:0.5%Cr^{3+} and $LaMgAl_{11}O_{19}$:20%Mn^{2+}, 0.5%Cr^{3+}

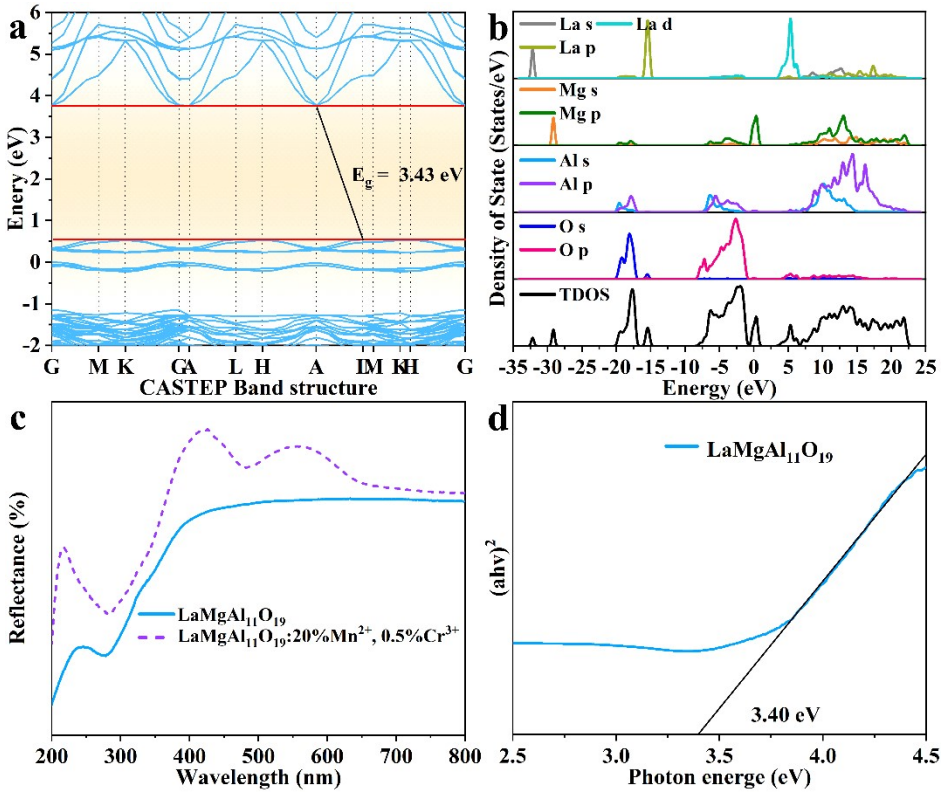

Fig. S5 Band structure (a) and total and partial DOS (b) of $LaMgAl_{11}O_{19}$, diffuse reflectance spectra of $LaMgAl_{11}O_{19}$ and $LaMgAl_{11}O_{19}$:20%Mn^{2+}, 0.5%Cr^{3+} (c) and band-gap energies of $LaMgAl_{11}O_{19}$ (d)

Computational Findings of Crystals Based on DFT

To gain further insight into the electronic structures of $LaMgAl_{11}O_{19}$, density functional theory (DFT) calculations are employed to estimate the band gap energy. **Fig. S5a** shows the calculated band structure of $LaMgAl_{11}O_{19}$. DFT calculation results of pure $LaMgAl_{11}O_{19}$ exist the exact conduction band bottom at A point and valance band maximum at L point, which suggests it is an indirect band gap with ~3.43 eV value. The calculated value is quite close to the optical band gap value of ~3.4 eV. **Fig. S5b** shows the total and partial densities of states (DOS) for different atoms, the conduction band minimum (CBM) of $LaMgAl_{11}O_{19}$ mainly contributed by La 5d orbitals and valance band maximum (VBM) is derived from by Mg 2p orbitals. The

bandgaps are calculated using the Kubelka-Munk function (equation (1) and (2)) based on the diffuse reflectance spectra (**Fig. S5c**):[1]

$$[F(R_\infty)hv]^n = C(hv - E_g) \quad (1)$$

$$F(R_\infty) = (1-R)^2/2R \quad (2)$$

Where hv represents photon energy, the value of exponent n indicates transition coefficient, n = 2 or 1/2 denotes the direct or indirect band gap respectively, $LaMgAl_{11}O_{19}$ belongs to indirect band gap, so n value is 1/2, C stands the proportionality constant, E_g signifies the band gap value, R is reflection coefficient. After calculation, the band gap of $LaMgAl_{11}O_{19}$ is 3.40 eV, and the electronic band structure of the sample can be corresponded to the optical band gap obtained by the absorption spectra (**Fig. S5d**), indicating that $LaMgAl_{11}O_{19}$ is suitable as a potential host.

As shown in **Fig. 3b**, the Tanabe-Sugano energy level diagram of Cr^{3+} in $LaMgAl_{11}O_{19}$ shows that the $^4T_{1g}$ and $^4T_{2g}$ energy levels strongly depend on the crystal field intensity, while the position of the ^2E_g energy level has little relationship with the crystal field intensity D_q. Therefore, the $^4A_{2g}\rightarrow{}^4T_{1g}$, $^4A_{2g}\rightarrow{}^4T_{2g}$ and $^2E_g\rightarrow{}^4A_{2g}$ levels energies of the $LaMgAl_{11}O_{19}$:0.5% Cr^{3+} are 23810cm^{-1}, 17319 cm^{-1} and 14025 cm^{-1}, respectively. According to equation (1), the local crystal field intensity D_q of Cr^{3+} in $LaMgAl_{11}O_{19}$ can be determined:[2, 3]

$$E(^4T_{2g}) = 10D_q (1)$$

For the $LaMgAl_{11}O_{19}$:0.5% Cr^{3+} sample, the Racah parameter B can be calculated to be 625 cm^{-1} using equation (2-3):[2, 3]

$$\Delta E = E(^4T_{1g}) - E(^4T_{2g}) (2)$$

$$\frac{D_q}{B} = \frac{15\left(\frac{\Delta E}{D_q} - 8\right)}{\left(\frac{\Delta E}{D_q}\right)^2 - 10\frac{\Delta E}{D_q}} (3)$$

Here, the energy difference between $^4T_{1g}$ and $^4T_{2g}$ is calculated as 6419 cm^{-1}.

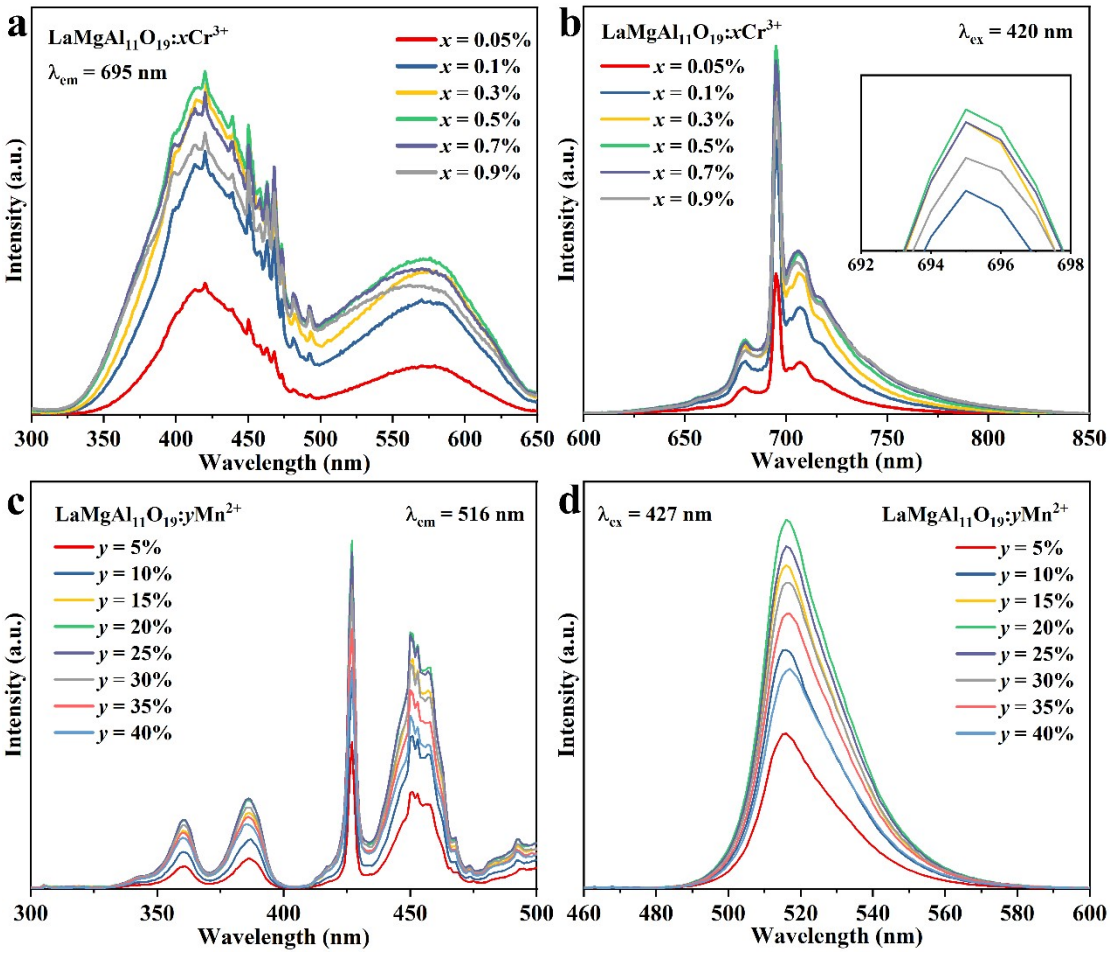

Fig. S6 Excitation and emission spectra of $LaMgAl_{11}O_{19}:xCr^{3+}$ (x = 0, 0.05%, 0.1%, 0.3%, 0.5%, 0.7% and 0.9%) (a and b) and $LaMgAl_{11}O_{19}:yMn^{2+}$ (y = 5%, 10%, 15%, 20%, 25%, 30%, 35% and 40%) (b and d)

In order to further determine the mechanism of concentration quenching, the critical distance (R_c) between adjacent Mn^{4+} ions will be calculated by equation (3):[4]

$$R_c \approx 2 \times \left[\frac{3V}{4\pi x_c N}\right]^{\frac{1}{3}} \qquad (3)$$

Here V represents the unit cell volume, $N$is the number of available sites of Cr^{3+} can substitute in the host and $x_c$stands the critical Cr^{3+} concentration in the matrix. For $LaMgAl_{11}O_{19}:Cr^{3+}$phosphor, V = 594.8 Å^3, x_c = 0.05 and N = 2. Therefore, the calculated R_c value is 22.47 Å, which is much higher than the critical value of the

interion exchange interaction and the electric multipole interaction (R_c = 5 Å), which means that the electric multipole interaction plays a dominant role in the occurrence of the concentration quenching phenomenon. Based on Dexter theory, the type of electric multipole interaction is further studied and the relationship between log(x) and log(I/x) is obtained by equation (4) and simplified equation (5).[5]

$$\frac{I}{x} = k\left[1 + \beta(x)^{\frac{\theta}{3}}\right]^{-1} \qquad (4)$$

$$log(I/x) = -\frac{\theta}{3}log(x) + A \qquad (5)$$

Where $I$is the photoluminescence intensity, $x$represents the Cr^{3+} concentration, and k and β are constants. A line with the slope of -0.74 (-θ/3) can be obtained by fitting, θ = 2.22 is closest to 6, so the concentration quenching mechanism is a dipole-dipole interaction.

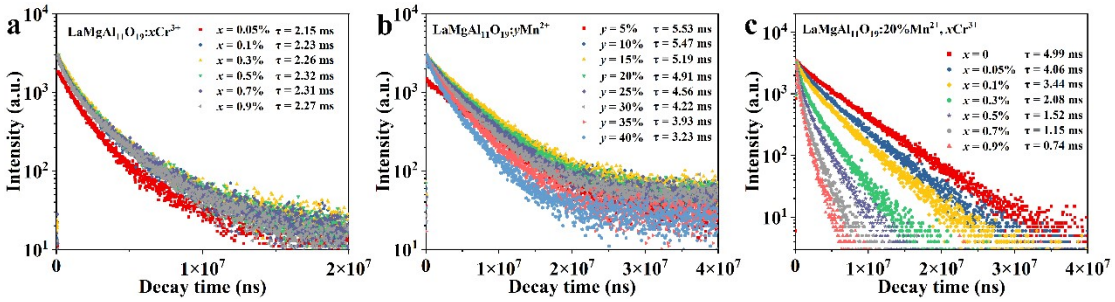

Fig. S7 Decay curves of $LaMgAl_{11}O_{19}$:$x$$Cr^{3+}$ (x = 0, 0.05%, 0.1%, 0.3%, 0.5%, 0.7% and 0.9%) (a), $LaMgAl_{11}O_{19}$:$y$$Mn^{2+}$ (y = 5%, 10%, 15%, 20%, 25%, 30%, 35% and 40%) (b) and $LaMgAl_{11}O_{19}$:20%Mn^{2+}, $x$$Cr^{3+}$ (x = 0, 0.05%, 0.1%, 0.3%, 0.5%, 0.7% and 0.9%) under 427 nm excitation and 625 nm monitoring

Accordingly, as shown in **Fig. S6a** and **b**, under 420 nm excitation and 695 nm monitoring and 427 nm excitation and 516 nm monitoring, the fluorescence decay curves of a series of green phosphors with different $Cr^{3+}$and Mn^{2+}ions doping concentrations were fitted by double exponential equation (6)-(7):[6]

$$I_t = I_0 + A_1 exp^{\left(-t/\tau_1\right)} + A_2 exp^{\left(-t/\tau_2\right)} \qquad (6)$$

$$\tau^* = \frac{A_1\tau_1^2 + A_2\tau_2^2}{A_1\tau_1 + A_2\tau_2} \qquad (7)$$

where $I_{(t)}$ and I_0 represent the emission intensity at moment t and initial fluorescence intensity of the as-prepared samples, A_1 and $A_2$are a constant, andτ_1 and $\tau_2$denote the fluorescence decay time, τ^* stands for average lifetime.

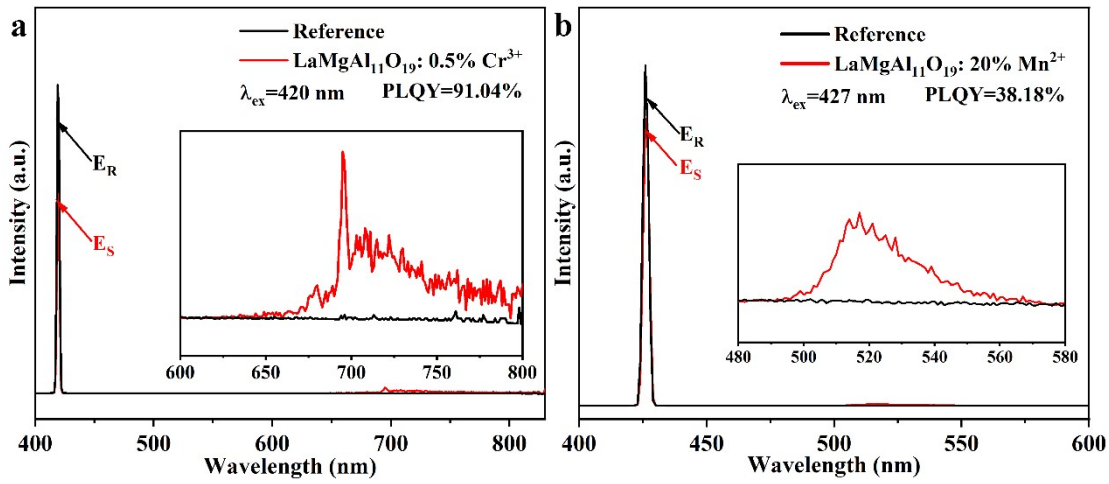

Fig. S8 PLQY spectra of LMAO:0.5%Cr^{3+} (λ_{ex} = 420 nm, Scatter Range: 409.00 to 429.00 nm, Emission Range: 617.00 to 847.00 nm) (a) and LMAO:20%Mn^{2+} (λ_{ex} = 427 nm, Scatter Range: 414.00 to 436.00 nm, Emission Range: 492.00 to 576.00 nm) (b)

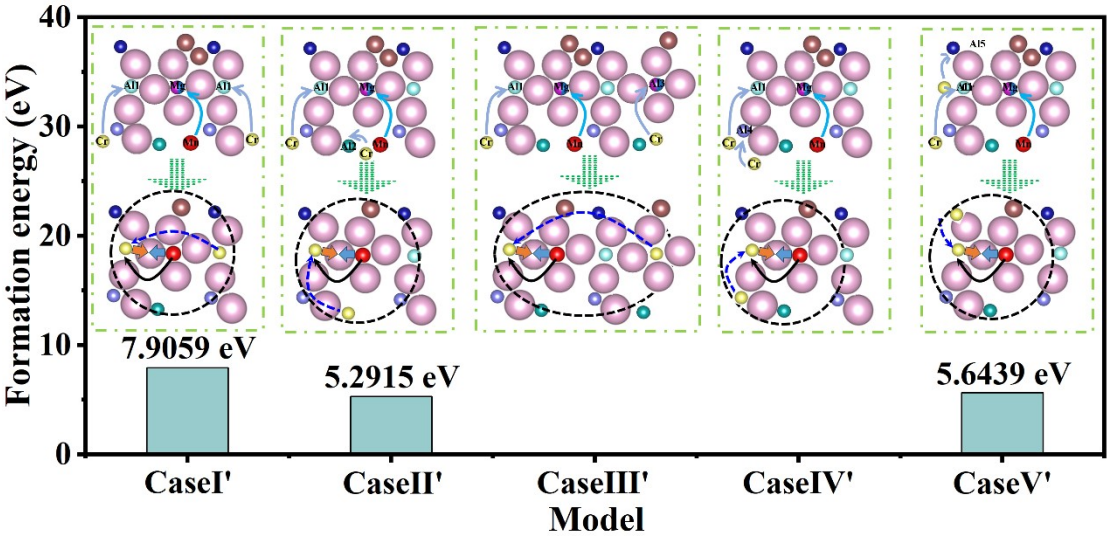

Fig. S9 Formation energy diagram comparing each available doping model in LMAO:Mn^{2+}, Cr^{3+} (Cr^{3+}-Cr^{3+} ion pairs)

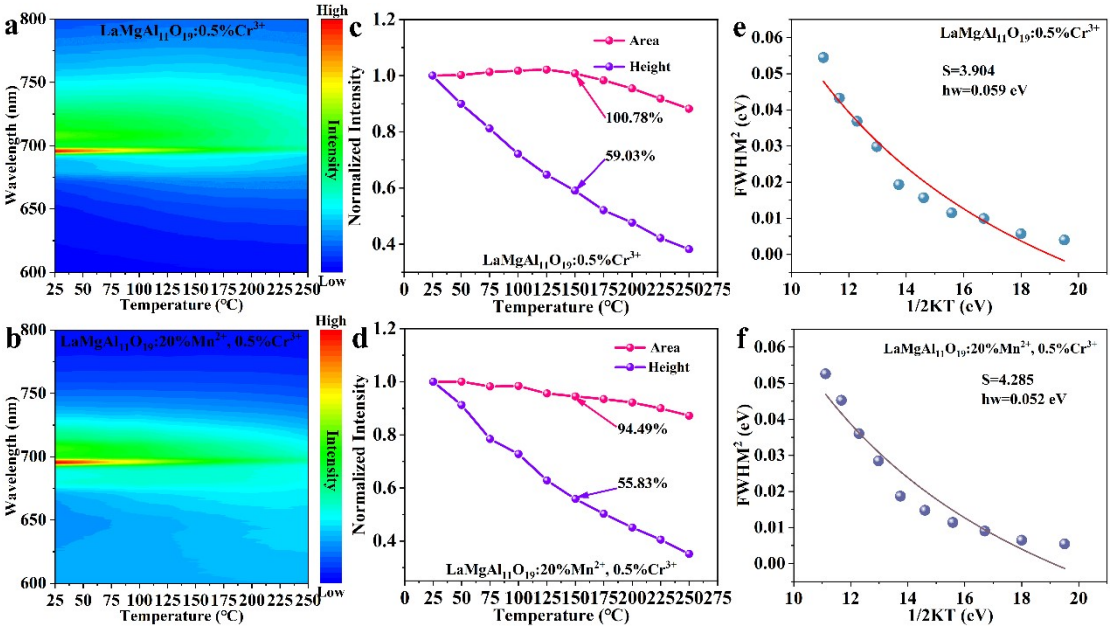

Fig. S10 Temperature-dependent emission spectra, relative intensity and fitting curve of $FWHM^2$ versus 1/2kT of $LaMgAl_{11}O_{19}:0.5\%Cr^{3+}$ (a, c and e) and $LaMgAl_{11}O_{19}:20\%Mn^{2+}$, $0.5\%Cr^{3+}$ (b, d and f)

Table S1 Cell parameters of LMAO:xCr^{3+} (x = 0, 0.05%, 0.1%, 0.3%, 0.5%, 0.7% and 0.9%) samples

Sample	Crystal structure	Space group	Cell parameters		
			$a = b$ (Å)	c (Å)	V (Å^3)
LMAO	Hexagonal	P63/mmc (194)	5.592	21.965	594.8
LMAO:0%Cr^{3+}	Hexagonal	P63/mmc (194)	5.593	21.945	594.40
LMAO:0.05%Cr^{3+}	Hexagonal	P63/mmc (194)	5.593	21.939	594.25
LMAO:0.1%Cr^{3+}	Hexagonal	P63/mmc (194)	5.591	21.950	594.16
LMAO:0.3%Cr^{3+}	Hexagonal	P63/mmc (194)	5.590	21.946	593.93
LMAO:0.5%Cr^{3+}	Hexagonal	P63/mmc (194)	5.590	21.948	593.88
LMAO:0.7%Cr^{3+}	Hexagonal	P63/mmc (194)	5.590	21.948	593.87
LMAO:0.9%Cr^{3+}	Hexagonal	P63/mmc (194)	5.590	21.941	593.78

Table S2 Cell parameters of LMAO:yMn^{2+} (y = 0%, 5%, 10%, 15%, 20%, 25%, 30%, 35% and 40%) samples

Sample	Crystal structure	Space group	Cell parameters		
			$a = b$ (Å)	c (Å)	V (Å^3)
LMAO	Hexagonal	P63/mmc (194)	5.592	21.965	594.80
LMAO:0%Mn^{2+}	Hexagonal	P63/mmc (194)	5.588	21.922	592.83
LMAO:5%Mn^{2+}	Hexagonal	P63/mmc (194)	5.589	21.943	593.66
LMAO:10%Mn^{2+}	Hexagonal	P63/mmc (194)	5.589	21.944	593.71
LMAO:15%Mn^{2+}	Hexagonal	P63/mmc (194)	5.591	21.938	593.89
LMAO:20%Mn^{2+}	Hexagonal	P63/mmc (194)	5.591	21.944	594.12
LMAO:25%Mn^{2+}	Hexagonal	P63/mmc (194)	5.591	21.955	594.40
LMAO:30%Mn^{2+}	Hexagonal	P63/mmc (194)	5.591	21.959	594.45
LMAO:35%Mn^{2+}	Hexagonal	P63/mmc (194)	5.592	21.953	594.51
LMAO:40%Mn^{2+}	Hexagonal	P63/mmc (194)	5.593	21.959	594.78

Table S3 Cell parameters of , and LMAO:20%Mn^{2+}, *x*Cr^{3+} (*x* = 0, 0.05%, 0.1%, 0.3%, 0.5%, 0.7% and 0.9%) samples

Sample	Crystal structure	Space group	Cell parameters		
			a = *b* (Å)	*c* (Å)	*V* (Å^3)
LMAO	Hexagonal	P63/mmc (194)	5.592	21.965	594.80
LMAO:20%Mn^{2+}, 0%Cr^{3+}	Hexagonal	P63/mmc (194)	5.594	21.954	594.88
LMAO:20%Mn^{2+}, 0.05%Cr^{3+}	Hexagonal	P63/mmc (194)	5.592	21.955	594.51
LMAO: 20%Mn^{2+}, 0.1%Cr^{3+}	Hexagonal	P63/mmc (194)	5.593	21.957	594.73
LMAO: 20%Mn^{2+}, 0.3%Cr^{3+}	Hexagonal	P63/mmc (194)	5.592	21.948	594.42
LMAO: 20%Mn^{2+}, 0.5%Cr^{3+}	Hexagonal	P63/mmc (194)	5.593	21.960	594.84
LMAO: 20%Mn^{2+}, 0.7%Cr^{3+}	Hexagonal	P63/mmc (194)	5.592	21.953	594.50
LMAO: 20%Mn^{2+}, 0.9%Cr^{3+}	Hexagonal	P63/mmc (194)	5.590	21.938	593.68

Table S4 Refined structural parameters of $LaMgAl_{11}O_{19}$:0.1%Cr^{3+}

	Atom	x	y	z	Occ.	Site		
1	Al1	0.000	0.000	0.000	0.700	2*a*	space	$P6_3/mmc$
2	Mg1	0.000	0.000	0.000	0.250	2*a*	group	(194)
3	Cr1	0.000	0.000	0.000	0.050	2*a*		
4	Ga2	0.000	0.000	0.241(3)	0.500	4*e*		
5	Ga3	0.333	0.666	0.026(8)	0.625	4*f*	symmetry	hexagonal
6	Mg3	0.333	0.666	0.026(8)	0.375	4*f*		
7	Ga4	0.333	0.666	0.188(4)	0.800	4*f*	Lattice parameters (Å)	*a*=*b* = 5.805
8	Cr4	0.333	0.666	0.188(4)	0.200	4*f*		*c*=22.702
9	Ga5	0.833(3)	0.166(7)	0.108(3)	0.890	12*k*		
10	Cr5	0.833(3)	0.166(7)	0.108(3)	0.110	12*k*		
11	O1	0.000	0.000	0.150(3)	1.000	4*e*		
12	O2	0.666	0.333	0.057(9)	1.000	4*f*	R_p	8.115
13	O3	0.182(0)	-0.182(0)	0.250	1.000	6*h*	R_w	10.243
14	O4	0.152(0)	-0.152(0)	0.053(3)	1.000	12*k*	R_{exp}	5.117
15	O5	0.505(0)	-0.505(0)	0.151(3)	1.000	12*k*		
16	La1	0.666	0.333	0.250	0.770	2*d*		
17	La2	0.732(3)	0.267(7)	0.250	0.076	6*h*		

Table S2 Important photoelectric parameters of the WLED device under different driving currents (50-400 mA).

Device	Current (mA)	R_a	*CCT* (K)	CIE (x,y)	Luminous efficiency ($lm \cdot W^{-1}$)
WLED	50	89.0	4888	(0.3499, 0.3686)	68.93
	100	90.5	4890	(0.3502, 0.3721)	64.47
	150	91.5	4896	(0.3502, 0.3743)	60.33
	200	91.4	4942	(0.3487, 0.3731)	53.92
	250	92.4	4992	(0.3472, 0.3728)	51.80
	300	94.2	5030	(0.3464, 0.3762)	52.43
	350	94.6	5080	(0.3449, 0.3765)	50.53
	400	91.9	5250	(0.3394, 0.3658)	42.63

References

1. H. Wang, Y.X. Pan, Y.H. Ding, H.Z. Lian, J. Lin, L.Y. Li, *Adv. Opt. Mater*., **2024**, 12(24) 2400935.

2. P. Zhang, Z.W. Luo, X.Y. Liu, P. He, S.X. Liu, W.C. Lei, H.Z. Liang, Z.Y. Zhou, A.X. Lu, *J. Alloys Compd*., **2022**, 926 166844.

3. F.Q. He, E.H. Song, Y.Y. Zhou, H. Ming, Z.T. Chen, J.C. Wu, P.S. Shao, X.F. Yang, Z.G. Xia, Q.Y. Zhang, *Adv. Funct. Mater*., **2021**, 31(36) 2103743.

4. M. Zhang, P.P. Dang, Y.J. Wan, Y.S. Wang, Z.X. Zeng, D.J. Liu, Q.Q. Zhang, G.G. Li, J. Lin, *Adv. Opt. Mater*., **2024**, 12(15) 2302941.

5. G. Sivakumar, A.T.M. Munthasir, P. Thilagar, S. Natarajan, *Chem. Mater*., **2024**, 36(11) 5356-5369.

6. X.Y. Dai, X.K. Zou, H.R. Zhang, W.B. Chen, C.W. Yang, M.S. Molokeev, Z.G. Xia, Y.L. Liu, X.J. Zhang, M.T. Zheng, B.F. Lei, *Adv. Opt. Mater*., **2024**, 12 2302380.